

Dendrite Suppression in Zn Batteries Through Hetero-Epitaxial Residual Stresses Shield

Musanna Galib,[†] Amardeep Amardeep,[‡] Jian Liu,^{*,‡} and Mauricio Ponga^{*,†}

[†]*Department of Mechanical Engineering, The University of British Columbia, 2054 - 6250
Applied Science Lane, Vancouver, BC, V6T 1Z4, Canada*

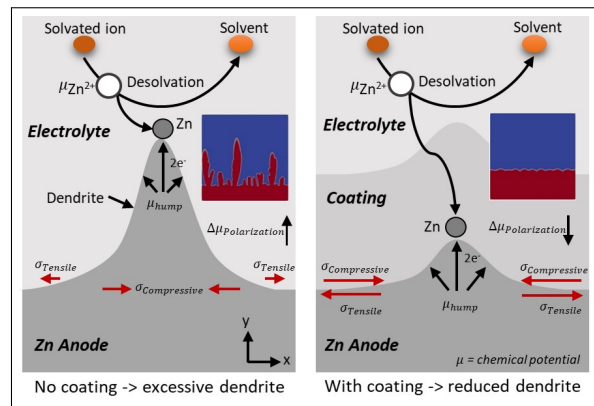
[‡]*School of Engineering, Faculty of Applied Science, The University of British Columbia,
Okanagan Campus, Kelowna, BC, V1V 1V7, Canada*

E-mail: jian.liu@ubc.ca; mponga@mech.ubc.ca

Abstract

Dendrite formation is a long-standing problem for the commercial application of aqueous zinc (Zn)-ion batteries (AZIB). Here, we investigate the effect of hetero-epitaxial residual stresses due to layered coatings on dendrite suppression. We found that atomic and molecular layered coatings can substantially reduce dendritic growth in AZIB by providing shielding due to residual stresses, even at single and a few layers of coatings. Through a combined experimental and numerical approach, we demonstrate that the residual stresses developed due to the coating of the Zn anodes significantly reduced the chemical potential polarization around dendrite embryos, forcing the deposition of zinc in the regions adjacent to the protuberances. This, in turn, results in a slower rate of dendritic growth, and eventually, dendrite suppression. The fundamental understanding of the effect of residual stresses due to coatings demonstrated herein can be extended to various metal anode batteries such as Li or Na.

TOC Graphic



Introduction

Rechargeable metal anode batteries with, such as Zn,¹ Na,² Al,³ Ca,⁴ stand out as favorable contenders for the next-generation energy storage devices. Their attractiveness stems from their excellent gravimetric energy density, low redox potential, cost-effectiveness, and enhanced safety characteristics.⁵ However, a common obstacle hindering the widespread adoption of these metal anode-based batteries is the challenge posed by suboptimal cycling performance and safety concerns, specifically linked to dendrite growth.⁶

Zn metal offers notable advantages, including substantial capacity (820 mAh·g⁻¹ and 5848 Ah·L⁻¹ of Zn compared to 3861 mAh·g⁻¹ and 2061 Ah·L⁻¹ of Li),⁷ greater concentration in the earth’s crust (70 ppm of Zn compared to 20 ppm of Li),⁸ and cost-effectiveness (USD 1.8 – 4 per kg of Zn compared to USD 5.8 – 80 per kg of Li).⁹ These factors have spurred the current revival of rechargeable aqueous Zn ion batteries (AZIBs), known for their safety and affordability (< USD 10 per kWh of AZIBs¹⁰ compared to USD 135 per kWh of LIBs).¹¹ However, akin to Li metal, anodic insufficiency remains a persistent challenge in AZIBs due to dendritic Zn growth, Zn passivation and corrosion, and H₂ evolution.¹² Zn dendrites, usually deemed as the primary reason for internal short-circuits in AZIBs, proliferate next to the separator, eventually breaching the separator. Identical to Li, the distal ends of Zn dendrites undergo passivation, resulting in “dead” Zn. This accumulation leads to electrolyte insufficiency, anodic capacity loss, increased cell resistance and polarization.¹³ Impurities in Zn give rise to by-products, such as Zn(OH)₂ or Zn₄SO₄(OH)₆·nH₂O, in electrolytes alongside gas evolution. These problems are rooted in the same source: an unfavorable interaction at the anode and electrolyte contact.¹²

The electroplating of Zn involves a sequence of events encompassing Zn²⁺ ion diffusion and migration, then reduction and nucleation, and finally, crystal growth. As a diffusion-controlled process, Zn nucleation is influenced by the applied electric field and, hence, ion distribution.¹⁴ The evolution of Zn dendrites is perpetuated by inhomogeneous nucleation due to the localized high electric field and preferential accumulation at the tips with large

curvature radii.¹⁵ However, the pivotal roles are played by electrochemical operational requirements such as current density and plating/stripping capacity in shaping the dendritic structure of Zn.¹⁶ Recent studies have utilized various techniques to investigate crystal structures, for instance, examining nanoscale or microscale forms of dendrites through ex-situ electron microscopy and observing lateral morphological growth of the Zn anode via in-situ optical microscopy (OM).¹⁷ Furthermore, surface coatings could be an effective strategy to suppress dendrite growth in metallic anodes by providing nucleation uniformity^{18–20}.

Here, we demonstrate how residual stresses can suppress dendrite nucleation and growth by altering the chemical potential near the neighborhood of dendrite embryos. First, we performed an operando investigation of dendritic growth in Zn||Zn symmetric cells through in-situ OM to correlate the microstructure evolution and electrochemical conditions, specifically in thin films. Further, to unveil the dendrite formation mechanics based on these experiments, a mesoscale simulation technique using phase-field modeling (PFM)²¹ was used to capture the dendrite evolution under various levels of residual stresses.

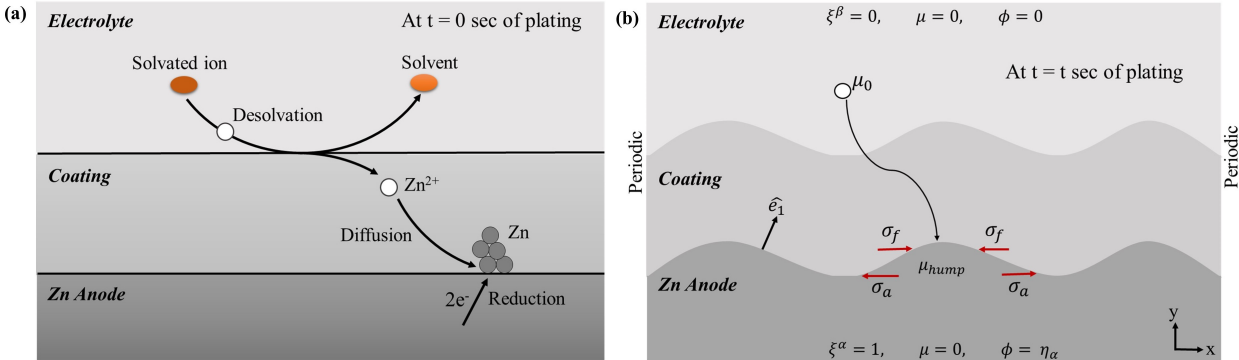


Figure 1: (a) Schematic diagram illustrating the electrodeposition of zinc ion on the zinc metal anode under the effect of the coating. Here, the dark orange circle represents solvated ion, the light orange circle represents solvent, the dark ash represents metallic Zn, and the white circles represent Zn-ions; (b) boundary conditions for chemical potential (μ), electric potential (ϕ), and order parameter (ξ) associated with the electrochemical phenomena illustrated in (a) along with a schematic of reduction of dendritic growth due to coating due to the impact of thin-film/coating (σ_f) and anode stress (σ_a).

Results and Discussion

To illustrate the effect of the residual stresses during Zn deposition, we describe the process in the neighborhood of the thin film free-surface, where zinc ions leave their solvent molecules, as shown in Fig. 1(a), and settle on the thin film layer's top surface. The Zn ion then diffuses via the thin film layer. When the Zn-ion reaches the Zn metal-thin film interface, it is reduced, and direct deposition on the Zn metal surface is followed by two-electron transfer. Since the interface is flat, there are no preferential sites and deposition happens randomly. However, surface roughness introduces preferred deposition sites via modification of the electric field originating humps or protuberances, ultimately nucleating dendrites (see Fig. 1(b)). Thus, the modified chemical potential (μ) along a heteroepitaxial thin film anode interface can be computed knowing the atomic volume Ω_0 as:

$$\mu = \mu_0 - (\sigma_x + \sigma_y)\Omega_0. \tag{1}$$

Here, μ_0 , is the chemical potential of deposited Zn ions, σ_x is the resultant in-plane and σ_y is the stress normal to the anode's surface. The residual stresses (σ_f , σ_a) evolving due to hetero-epitaxy,²² contributing to σ_x and σ_y , thus modifying the chemical potential (μ) and reducing the dendrite growth. Here, we include the effect of the hetero-epitaxial stress in an electro-chemo-mechanical PFM as shown in Fig. 1(b) and Eq. (S4)- details are included in the methods section in the Supporting Information (SI).

The in-plane interfacial stresses developed by atomic and molecular layered deposition (ALD/MLD) can influence prolonging smooth surface morphology of zinc electrodes, even at high current densities, according to the modified chemical potential shown in Eq. (S4). However, dendrites in real life are also influenced by other circumstances, such as charging time, and gas evolution, amongst other factors. Therefore, to investigate the effect of the interfacial stress (σ_f), we performed charging/discharging of bare Zn and coated thin films at a very high current density (details of the ALD/MLD coatings can be found in the Ex-

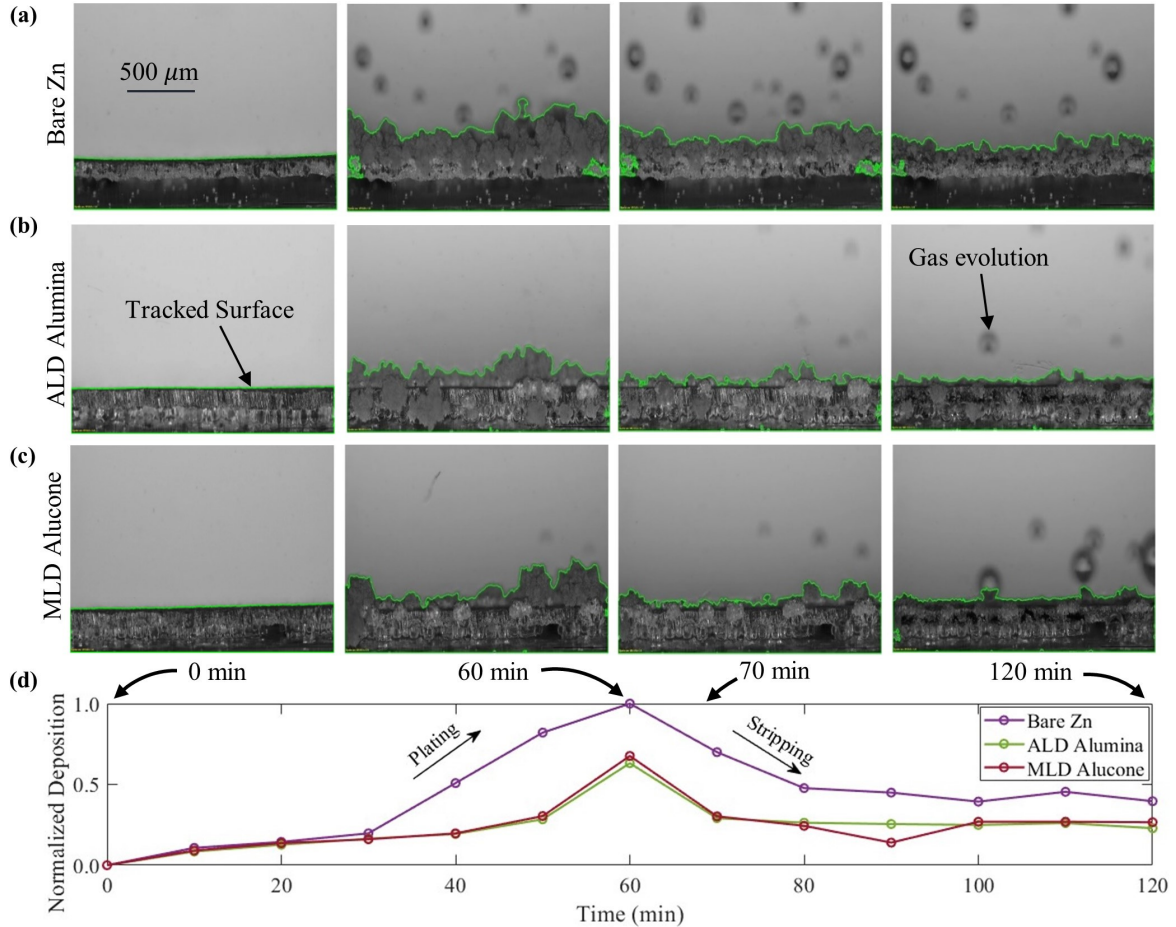


Figure 2: Operando imaging of the zinc plating (0-60 min) and stripping (61-120 min) under a current of 8 mA (current density of $10 \text{ mA} \cdot \text{cm}^{-2}$) to observe the morphological evolution for (a) bare Zn, (b) one layer (1C) ALD Alumina, and (c) MLD Alucone; (d) Time evolution of the normalized deposition during plating and stripping from pixel counts of OM images (a-c).

perimental Methods section of SI). Two different types of coatings were evaluated, including alumina and alucone, with different ALD/MLD cycles (one (1C), five (5C), ten (10C), and fifty (50C) cycles). Higher current density can easily stimulate Zn ion migration, affecting the deposition morphology and the coating effect will be more evident in this case. The dynamic process of Zn electrodeposition and dissolution in aqueous electrolytes was analyzed employing high-throughput operando OM at a consistent current of $10 \text{ mA} \cdot \text{cm}^{-2}$, as shown in Fig. 2. Fig. 2 (a) and Movie 1 (see SI) demonstrate the Zn electroplating in the bare Zn||Zn cell for 60 minutes of plating and 60 minutes of stripping. Fig. 2 (b) and Movie

2, along with Fig. 2 (c) and Movie 3, demonstrate the nucleation and growth of dendrites throughout the plating and stripping on an one layer (1C) alumina and alucone-coated Zn, respectively.

At time 0 minutes, no noticeable features were detected in Fig. 2(a,b,c). The system was in a state of equilibrium as described by the Nernst-Planck equation. A moss-like random dendritic Zn protrusions at 60 min were observed in all coated and uncoated cases, indicating irregular ion migration leads to Zn^{2+} ion aggregation and nucleation guided by the electric field.²³ Here, the bare Zn case had higher gas evolution and dendritic growth rate compared to the coated cases, as shown in Fig. 2. However, gas evolution increased with the increase of coating layers, as shown in Fig. S3. After 120 mins, due to irregular ion migration and uneven mass transport, the anode surfaces showed residual dendrites. Fig. 2 (d) depicts Zn's normalized deposition (area in each OM frame/maximum area), confirming the fact that the growth rate of the coated surfaces is slower than bare Zn, as the coated deposition is 37% lower after plating and 13% lower after stripping. To understand the surface roughness, the surface profiles were extracted and plotted in Fig. S4 (a). Similar to the normalized deposition, the uneven Zn^{2+} ion aggregation is higher for bare Zn after plating and stripping ends, as shown in Fig. S4 (b). Therefore, the OM experiments verify that the coating, which is as thin as just one ALD/MLD layer (1C), can significantly reduce dendritic growth rates. It is widely recognized that the formation of stresses inside solids can result in changes in their morphology. The equilibrium morphology and morphological stability of strained coating can be determined by balancing the elastic energy with the surface energy,²⁴ and here, the interfacial in-plane stress provides the surface energy to dictate the growth morphology.

As coating could be a barrier to the diffusion and migration process, we assessed the effect of coating on the cyclic performance of $\text{Zn}||\text{Zn}$ cells under a current density of $0.5 \text{ mA} \cdot \text{cm}^{-2}$, shown in Fig. 3(a). The cycle time of one layer (1C) ALD alumina before short-circuiting or electrolyte depletion (165 hr) is slightly higher than bare Zn (146 hr), whereas 1C MLD alucone carries stable charge-discharge voltage profiles for approximately 598 hr before facing

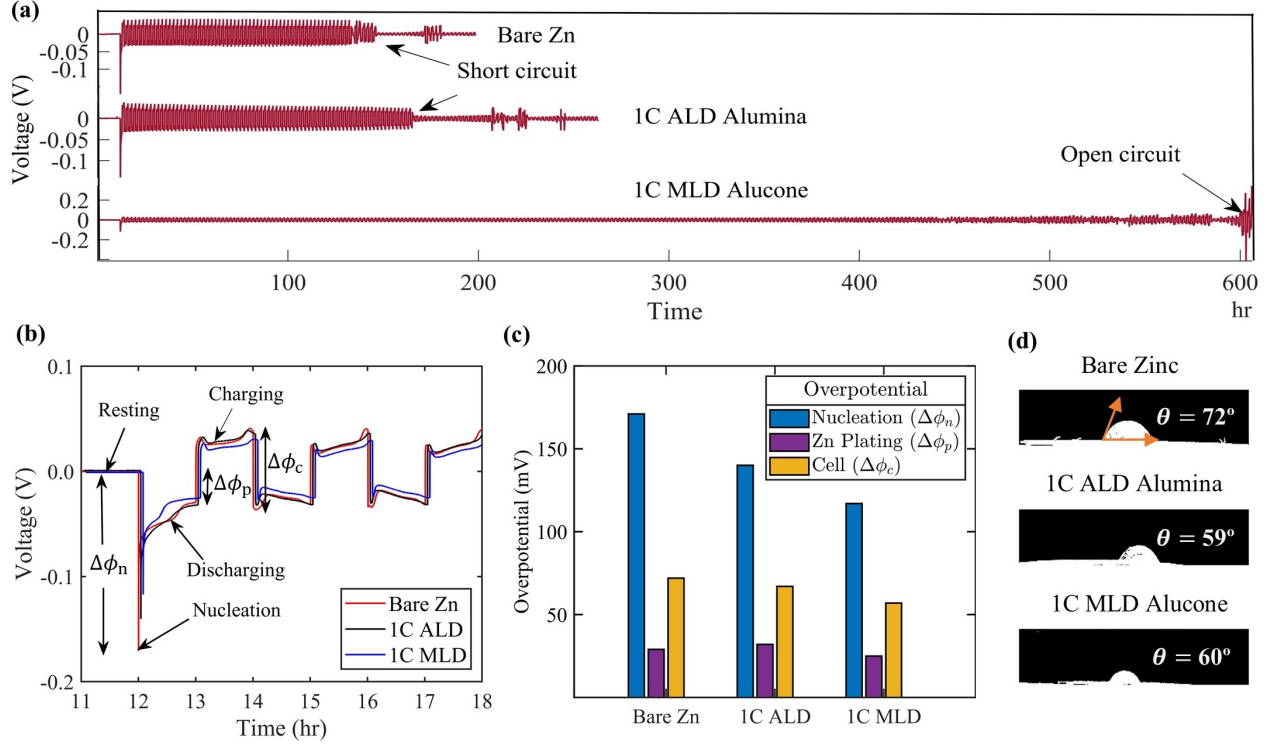


Figure 3: (a) Symmetric Zn||Zn cell charge-discharge profiles with bare Zn, one layer (1C) ALD alumina, one layer (1C) MLD Alucone coating at a current density of $10 \text{ mA} \cdot \text{cm}^{-2}$ until short- or open-circuiting at room temperature; (b,c) voltage (millivolts) profiles of first few cycles to observe the patterns of overpotentials; and (d) contact angle measurement for bare and coated Zn foils.

high voltage open-circuit. The results imply that the alucone coating not only reduces the gas evolution and dendrite growth rate but also significantly improves the Zn cyclic performance. Here, for alucone coating, one layer (1C) coating showed the peak cycling life, whereas ten layers (10C) alumina coating showed the peak performance, as shown in Fig. S5. This finding suggests a complex interplay between residual stresses, gas evolution and cycling performance in batteries. From Fig. 3(b), in the first discharge process after 12 hrs of resting, the required nucleation overpotential (ϕ_n) to begin the Zn plating and stripping is lower for coated Zn compared to bare Zn. The nucleation overpotential for bare Zn, alumina-coated, and alucone-coated cells were -171, -140, and -117 mV, respectively, as shown in Fig. 3(c). This result indicates that Zn^{2+} and e^- transfer resistance decreases with the one layer of coating as lower nucleation potential is required. This is possibly due to the favorable

interaction between the coating and electrolyte employed, whereas only one layer of the coating does not create any insulating behavior to increase the overpotential, as mentioned in previous studies.²⁵ Furthermore, the first plating overpotential (ϕ_p) to start Zn plating is lowest for alucone-coated Zn (25 mV) compared to bare Zn (29 mV), whereas alumina-coated Zn has the highest (32 mV). On the other hand, cell overpotential (ϕ_c) shows a similar trend to nucleation overpotential as - bare Zn (72 mV) > alumina coating (67 mV) > alucone coating (57 mV). Lower cell overpotential for coated surfaces indicates lower resistance in the batteries, hence better performance for the coated electrodes. The influence of wettability on the ALD alumina and MLD alucone-coated Zn anode was analyzed in a 3 M Zn(SO₃CF₃)₂ aqueous electrolyte by measuring contact angles (θ) as shown in Fig. 3(d). The contact angle of alumina-coated Zn ($\theta = 59^\circ$) and alucone-coated Zn ($\theta = 60^\circ$) were much lower than the contact angle of bare Zn ($\theta = 72^\circ$). This suggests that the coated Zn surfaces have improved wettability with the aqueous solution. The enhanced wettability (*i.e.*, lower contact angle, higher adhesion) is advantageous for Zn plating/stripping (cycling) reactions as it can facilitate a consistent flow of Zn ions over the interface between the electrode and electrolyte.²⁶ This, in turn, reduces the production of Zn dendrites and lowers the charge transfer resistance during battery cycling.

To demonstrate the impact of coating on dendrite formation using Eq. (S4), we applied the in-plane residual stress as initial interfacial stress, calculated from the heteroepitaxial lattice-misfit for a stable coating on Zn surface,^{22,27} modifying the classical Butler-Volmer equation^{21,28,29} (See theoretical formulation in SI). Here, the solvated ions gain electrons from the electrode surface during the reduction process (Reduced Zn \rightleftharpoons Oxidized Zn + 2e⁻) when the overpotential becomes larger than the nucleation energy barrier. As a result, they overcome the nucleation energy barrier and start depositing on those sites.³⁰ Initial Zn atoms will either freely diffuse to an energy-favorable location or aggregate with other freshly created Zn atoms on the anode surface to generate the initial Zn core.³¹ For the first 50 seconds, there was no undulation on the surface for both bare and coated Zn shown in Fig. 4

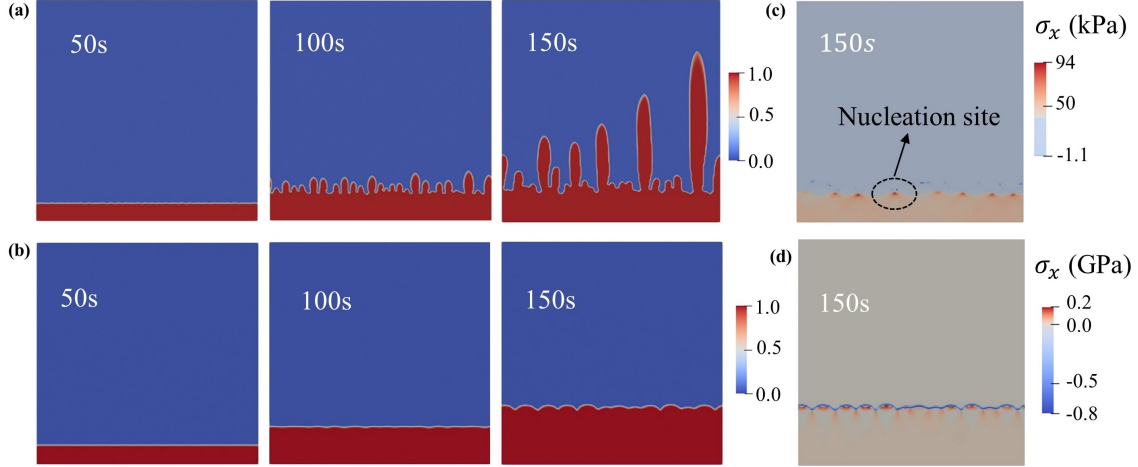


Figure 4: The development of dendrites (ξ), and the evolution of in-plane stress (σ_x) at an applied overpotential (ϕ) of 200 mV, current density (i) of $2.8 \text{ mA} \cdot \text{cm}^{-2}$, anode stress (σ_a) of 0.01 GPa, and anisotropy (δ) of 0.0 during 50, 100, and 150 seconds, respectively, for : (a, c) bare Zn, and (b, d) coated Zn. Here, the coated Zn represents both ALD and MLD coatings from the experiments.

(a), and Fig. 4 (b), respectively. At 100 seconds, bare Zn anodes had incipient dendrites formed, whereas, for coated Zn, the interface is pinned but no noticeable dendrites were formed. This suggests that while random dendrite nucleation could happen spontaneously, the residual stresses due to the coating suppresses the uncontrolled dendrite growth from the anode's surface. At 150 seconds, the bare Zn surface had prominent dendrites, whereas the coated Zn surface showed a slow dendritic growth rate. One of the reasons behind these inconsistent deposition phenomena is the chemical potential gradient (μ) as shown in Fig. S6. Zn^{2+} flux shown in Fig. S6 (a) can be explained according to the Nernst-Planck relationship, as Zn^{2+} diffusion can be caused by the concentration gradient, whereas Zn^{2+} migration can be caused by an electrostatic potential gradient. The ionic concentration near the anode swiftly drops except for the dendrite tip compared to that in the bulk electrolyte and thus creates a specific concentration gradient as shown in Fig. S6 (a).³² However, for the coated Zn case, due to the heteroepitaxial in-plane stress (about $\sigma_f = 1.2\text{-}1.3 \text{ GPa}$ for MLD Alucone, see Fig. S5), the chemical potential polarization is reduced as shown in Fig. S6 (b). This causes zinc ions to gather approximately uniformly at the anode surface without

favoring dendrite nucleation and growth. To elaborate, the derived interfacial stress has a significant impact on the dispersion of the zinc core’s morphology. The influence of the in-plane GPa range compressive stress shown in Fig. 4 (d) causes zinc ions close to the zinc anode’s surface to adsorb uniformly rather than clustering only in the nucleation sites. Zinc ions deposit readily at the tips of the zinc core, but the compressive stress over the tip of the protuberances is substantially stronger in suppressing the random growth of the Zn cores. On the other hand, as the in-plane stresses are low in the bare Zn surfaces, as shown in Fig. 4 (c), abundant charges are gathered over the tips due to the surface’s unevenness, where zinc ions are more prone to deposit. Therefore, tips are regarded as active sites for zinc deposition for bare Zn. As a result, the comparatively flat electrode surface promotes homogeneous Zn deposition while suppressing Zn dendrite formations, as shown in Fig. 4 (d).³¹

To further understand the role of the interfacial stress derived due to coating and the interplay with other cell parameters, we used different material anisotropy and current density to evaluate the effect of the stresses. In Fig. 5 (a,b,c), we fixed all parameters except δ (strength of anisotropy). While increasing δ gradually from zero (Fig. 4(a)) to 0.4 for bare Zn, we observed that the dendrite patterns shift from viscous fingering, *i.e.*, perfect isotropic growth ($\delta = 0.00, 0.04$, Fig. 5 (a)) to side branching ($\delta = 0.2, 0.4$, see Fig. 5 (b) and (c)). The non-symmetric side branching from principal branches increases with the increase of δ . However, for coated Zn, the growth of the principal dendritic branches starts late as δ increases, and no substantial dendrites were visible even at 150s, which explains the linear growth of the coated Zn as shown in Fig. 5 (d). Therefore, it is clear that initial interfacial stress due to coating is insensitive to δ and can suppress the dendritic growth.

Furthermore, the variation of current density can influence the Zn-ion concentration in the vicinity of the Zn anode shown in Fig. 5 (e,f,g). It is easier for zinc to nucleate unevenly with the high current because there will be a concentration gradient of zinc ions between the bulk solution and the reaction zone.³¹ As a result, for $i = 5 \text{ mA} \cdot \text{cm}^{-2}$, we saw sharp needle-

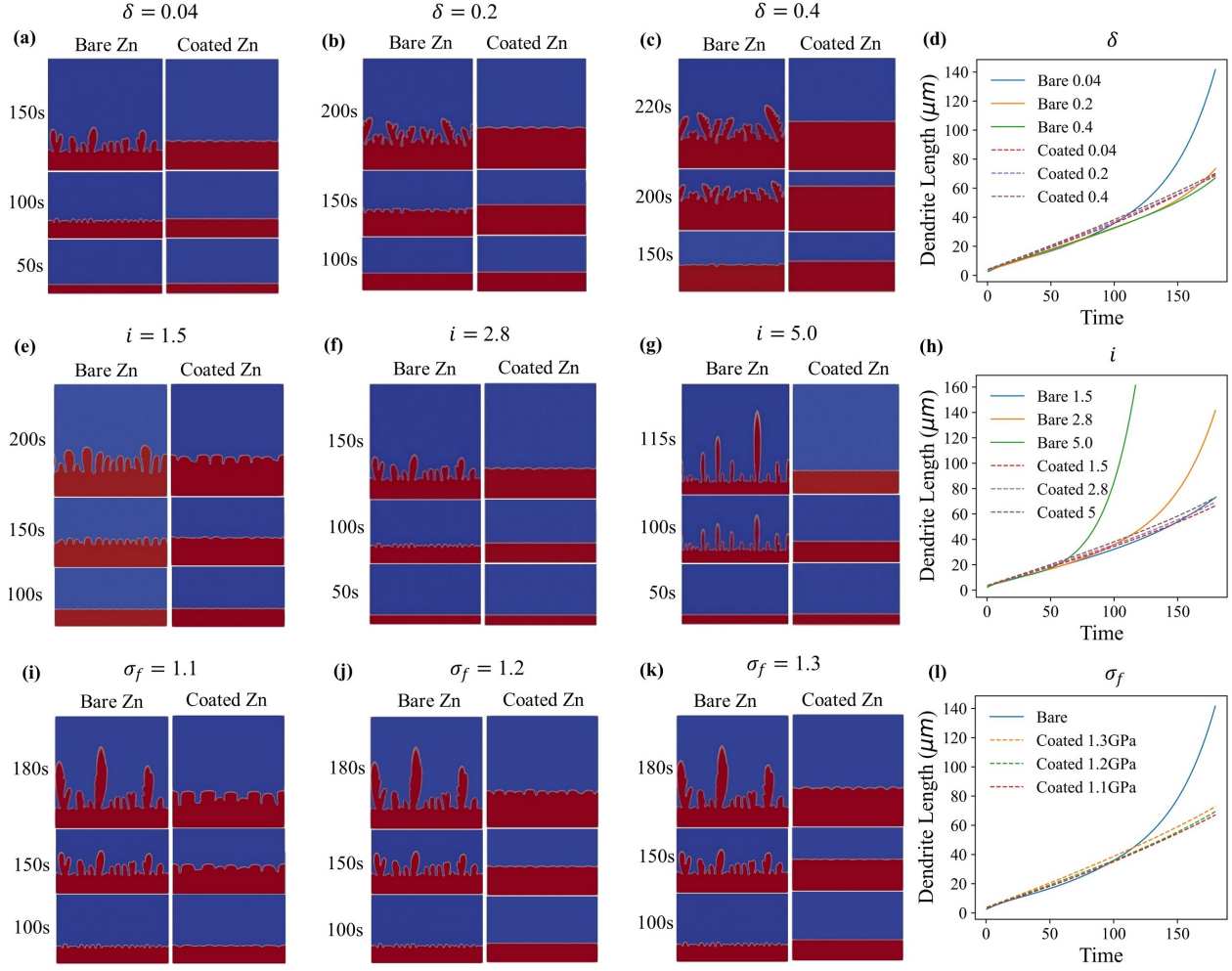


Figure 5: Morphology evolution for coated and bare Zn under the influence of different conditions: (a,b,c) anisotropy ($\delta = 0.04, 0.2, 0.4$), (e,f,g) current density ($i = 1.5, 2.8, 5.0 \text{ mA} \cdot \text{cm}^{-2}$), and (i,j,k) in-plane stress ($\sigma_f = 1.1, 1.2, 1.3 \text{ GPa}$); (d,h,l) average dendrite length with time evolution for all cases.

like dendrites only at 115s, whereas for $i = 1.5 \text{ mA} \cdot \text{cm}^{-2}$, finger-shaped dendrites started forming at 200s for bare Zn. For all current density variations, the coated Zn surface shows very low undulations on the surface due to the residual stresses. Next, Fig. 5 (i,j,k) shows the sensitivity of dendrite nucleation under variation of residual stress (σ_f) as there is drastic surface undulation at 150s for $\sigma_f = 1.1 \text{ GPa}$, whereas there is comparatively low undulation even at 180s for $\sigma_f = 1.2$ and 1.3 GPa . Here, Fig. 5 (d,h,l) indicates the average dendrite length with time and shows the exponential increase of dendrite tip for bare Zn compared to linear growth for coated cases for different anisotropy, current density, and interface stress.

Thus, numerical simulations confirmed that coating can reduce the dendrite growth rate in good agreement with in-situ experiments in Fig. 2.

Conclusion

By analyzing the bare and coated AZIB, we revealed an in-depth understanding of the influence of in-plane stress on altering chemical potential and, hence, suppressing dendrite growth. Firstly, using surface and area tracking of Zn dendrites, we found that subsequent dendrite growth and gas evolution are reduced by coating during Zn electrodeposition, even while applying very high current density. After the first cycle, the bare anode has significantly higher dead Zn and roughness compared to only one layer of ALD/MLD coating. Secondly, using phase-field modeling, we proved that the interfacial in-plane stresses arising from heteroepitaxial coating suppress the formation of sharp dendrites, whereas bare Zn electrodes show tip splitting, sharp fingers, and branching morphology depending on imposed anisotropy, and current density. Thus, our study demonstrates for the first time the effect of residual stresses due to hetero-epitaxial coatings on dendrite suppression and inhibition. Critically, we found that these stresses play a critical role in modifying the chemical potential near the surface of the anodes, resulting in a shielding mechanism to suppress dendrite growth. Remarkably, the effect of the residual stresses is robust under different current densities and anisotropy of the material, suggesting that the coating strategy of anodes can be an effective method to suppress dendrite growth in AZIB and possibly extendable to all-solid-state batteries.³³

Experimental Methods

Atomic and Molecular Layered Deposited (ALD/MLD) coatings

Zn foils (0.1 mm in thickness) were sliced into circular discs (diameter, $d = 14$ mm) and cleansed for 15 minutes by sonication successively in deionized (DI) water and alcohol, fol-

lowed by natural air drying. Alumina coating on the Zn foils was carried out at 100°C by alternatively providing trimethylaluminum (TMA) and H₂O, whereas alucone coating was performed by alternatively providing trimethylaluminum (TMA) and ethylene glycol (HO – CH₂ – CH₂ – OH) into a commercial GEMStar™ XT Atomic Layer Deposition System. The actuator keeps open to increase the pressure in the chamber and purges everything. When the actuator is closed, the chamber pressure stays at operating pressure (500-700 mTorr) when pulsing happens. The sequence for TMA pulsing is: 200 ms pulse of TMA, 5 s delay, delay 15 s (actuator opened), actuator closed. The sequence for the 2nd precursor (H₂O/EG) pulsing is: 21 ms pulse of H₂O/EG, 5 s delay, delay 15 s (actuator opened). Alumina and alucone coatings were applied to Zn foils with just 1 ALD/MLD (1C) cycle to get one layer of coating. Similarly, 5, 10, and 50 cycles (C) of the coating were applied for both alumina and alucone.

Battery Assembly, and Electrodeposition

Symmetric Zn||Zn coin cells were fabricated using Zn metal discs (d = 14 mm, thickness (h_s) 0.1 mm), separators (Whatman, glass fiber, GF/F, diameter d=19 mm), and 3 M Zn trifluoromethanesulfonate (Zn(SO₃CF₃)₂) aqueous electrolyte (75 μL). The coin cells were crimped with a hydraulic crimping machine at 1000 psi pressure. Galvanostatic charge/discharge tests for these two coating materials were conducted in a Neware battery testing system (Neware 4000). These tests, including all coated (1C, 5C, 10C, 50C) and bare Zn cases, were carried out at a fixed current density (j) of 0.5 mA · cm⁻² to analyze the cycling performance of AZIBs. All batteries were tested at room temperature (25 °C).

Operando Optical Microscopy and Batch Image Processing

Using an optical microscope (Olympus BX53M, Japan), in-situ monitoring of symmetric Zn||Zn cell's dendrite evolution and dissolution was carried out. A 5× objective lens was employed to achieve a natural aperture of 0.15 and a resolution of about 3.35 μm. Elec-

trochemical tests with high constant current density modes ($10 \text{ mA}\cdot\text{cm}^{-2}$, 8 mA over 8×10 mm electrode) were synchronized with picture collection. Digital photographs were taken constantly each minute for the first two to five cycles to record the dynamic growth until the screen got blurred. The electrochemical data is stored every 4 seconds. Subsequently, the captured images were converted from RGB to 8-bit images. To facilitate faster image processing to analyze the dynamic growth, datasets were batch-processed and tracked employing an open-source software named SurfTrack, using a color threshold between dendrites and background after binarization. The dendrite area and Zn dendrite height (surface roughness) were also quantified using SurfTrack.

Supporting Information Available

This material is available free of charge via the Internet at <https://pubs.acs.org>.

- List of symbols, Theoretical Formulation of the Phase-Field Method, Computational Implementation; Results: In-situ optical microscopy for multiple coated layers, Cyclic test for multiple coated layers, and Chemical potential evolution.
- Dendrite growth under in-situ optical microscopy for Bare Zn, 1C ALD Alumina and 1C MLD Alucone are added as movie, namely, `movie1_Bare_Zn.mp4`, `movie2_1C_ALD_Alumina.mp4`, and `movie3_1C_MLD_Alucone.mp4`, respectively.

Code Availability

- All post-processing of in-situ optical microscopy images to capture dendrite length and normalized deposition is done using the “SurfTrack” python package built available at: <https://github.com/MusannaGalib/SurfTrack>.
- All post-processing of MOOSE simulation’s exodus file format is done using the “MOOSEanalyze” python package built on Paraview’s PvPython and available at:

<https://github.com/MusannaGalib/MOOSEanalyze>.

Data Availability

All cycling data (Bare Zn, 1C ALD Alumina, 1C MLD Alucone) is available at:

<https://github.com/MusannaGalib/MOOSEanalyze/tree/main/CyclicTest>.

Author Contributions

Musanna Galib: Conceptualization, Investigation, Software, Formal analysis, Data Curation, Validation, Writing - Original Draft, Writing - Review & Editing. **Amardeep Amardeep:** Investigation, Writing - Review & Editing. **Jian Liu:** Investigation, Writing - Review & Editing, Supervision, Funding acquisition. **Mauricio Ponga:** Conceptualization, Investigation, Writing - Review & Editing, Supervision, Project administration, Funding acquisition.

Acknowledgement

We acknowledge the support from the New Frontiers in Research Fund (NFRFE-2019-01095), the Discovery grant from the Natural Sciences and Engineering Research Council of Canada (NSERC) under Award Application Number 2016-06114, Collaborative Research Mobility Award (UBC CRMA) and the UBC Eminence program (Battery Innovation Cluster). M.G. gratefully acknowledges the financial support from the Department of Mechanical Engineering at UBC through the Four Years Fellowship. This research was supported through high-performance computational resources and services provided by Advanced Research Computing at the University of British Columbia. M.G. would also like to express gratitude to Biswajeet Rath for the helpful discussions about phase-field modeling and Zhenrui Wu for the helpful discussions about electrochemical experiments.

References

- (1) Parker, J. F.; Ko, J. S.; Rolison, D. R.; Long, J. W. Translating Materials-Level Performance into Device-Relevant Metrics for Zinc-Based Batteries. *Joule* **2018**, *2*, 2519–2527.
- (2) Bauer, A.; Song, J.; Vail, S.; Pan, W.; Barker, J.; Lu, Y. The Scale-up and Commercialization of Nonaqueous Na-Ion Battery Technologies. *Advanced Energy Materials* **2018**, *8*, 1702869.
- (3) Lin, M.-C. et al. An ultrafast rechargeable aluminium-ion battery. *Nature* **2015**, *520*, 324–328.
- (4) Ouchi, T.; Kim, H.; Spatocco, B. L.; Sadoway, D. R. Calcium-based multi-element chemistry for grid-scale electrochemical energy storage. *Nature Communications* **2016**, *7*, 10999.
- (5) Zhang, X.; Lv, R.; Tang, W.; Li, G.; Wang, A.; Dong, A.; Liu, X.; Luo, J. Challenges and Opportunities for Multivalent Metal Anodes in Rechargeable Batteries. *Advanced Functional Materials* **2020**, *30*, 2004187.
- (6) Wood, K. N.; Noked, M.; Dasgupta, N. P. Lithium Metal Anodes: Toward an Improved Understanding of Coupled Morphological, Electrochemical, and Mechanical Behavior. *ACS Energy Letters* **2017**, *2*, 664–672.
- (7) Winter, M.; Barnett, B.; Xu, K. Before Li Ion Batteries. *Chemical Reviews* **2018**, *118*, 11433–11456.
- (8) Yaroshevsky, A. A. Abundances of chemical elements in the Earth’s crust. *Geochemistry International* **2006**, *44*, 48–55.
- (9) Innocenti, A.; Bresser, D.; Garche, J.; Passerini, S. A critical discussion of the current

- availability of lithium and zinc for use in batteries. *Nature Communications* **2024**, *15*, 4068.
- (10) Chao, D.; Zhou, W.; Ye, C.; Zhang, Q.; Chen, Y.; Gu, L.; Davey, K.; Qiao, S.-Z. An Electrolytic Zn – MnO₂ Battery for High-Voltage and Scalable Energy Storage. *Angewandte Chemie International Edition* **2019**, *58*, 7823–7828.
- (11) Schmidt, O.; Hawkes, A.; Gambhir, A.; Staffell, I. The future cost of electrical energy storage based on experience rates. *Nature Energy* **2017**, *2*, 17110.
- (12) Wu, Z.; Zou, J.; Li, Y.; Hansen, E. J.; Sun, D.; Wang, H.; Wang, L.; Liu, J. Regulating Zinc Nucleation Sites and Electric Field Distribution to Achieve High-Performance Zinc Metal Anode via Surface Texturing. *Small* **2023**, *19*, 2206634.
- (13) Chen, K.-H.; Wood, K. N.; Kazyak, E.; LePage, W. S.; Davis, A. L.; Sanchez, A. J.; Dasgupta, N. P. Dead lithium: mass transport effects on voltage, capacity, and failure of lithium metal anodes. *J. Mater. Chem. A* **2017**, *5*, 11671–11681.
- (14) Wan, F.; Zhou, X.; Lu, Y.; Niu, Z.; Chen, J. Energy Storage Chemistry in Aqueous Zinc Metal Batteries. *ACS Energy Letters* **2020**, *5*, 3569–3590.
- (15) Yang, Q.; Li, Q.; Liu, Z.; Wang, D.; Guo, Y.; Li, X.; Tang, Y.; Li, H.; Dong, B.; Zhi, C. Dendrites in Zn-Based Batteries. *Advanced Materials* **2020**, *32*, 2001854.
- (16) Yang, Q.; Liang, G.; Guo, Y.; Liu, Z.; Yan, B.; Wang, D.; Huang, Z.; Li, X.; Fan, J.; Zhi, C. Do Zinc Dendrites Exist in Neutral Zinc Batteries: A Developed Electrohealing Strategy to In Situ Rescue In-Service Batteries. *Advanced Materials* **2019**, *31*, 1903778.
- (17) Du, W.; Zhang, Z.; Iacoviello, F.; Zhou, S.; Owen, R. E.; Jervis, R.; Brett, D. J. L.; Shearing, P. R. Observation of Zn Dendrite Growth via Operando Digital Microscopy and Time-Lapse Tomography. *ACS Applied Materials & Interfaces* **2023**, *15*, 14196–14205, PMID: 36892017.

- (18) Ren, Q.; Tang, X.; Zhao, X.; Wang, Y.; Li, C.; Wang, S.; Yuan, Y. A zincophilic interface coating for the suppression of dendrite growth in zinc anodes. *Nano Energy* **2023**, *109*, 108306.
- (19) Chen, P. et al. An Artificial Polyacrylonitrile Coating Layer Confining Zinc Dendrite Growth for Highly Reversible Aqueous Zinc-Based Batteries. *Advanced Science* **2021**, *8*, 2100309.
- (20) Zhang, Z.; Wu, L.; Zhou, D.; Weng, W.; Yao, X. Flexible Sulfide Electrolyte Thin Membrane with Ultrahigh Ionic Conductivity for All-Solid-State Lithium Batteries. *Nano Letters* **2021**, *21*, 5233–5239, PMID: 34106717.
- (21) Hong, Z.; Viswanathan, V. Phase-Field Simulations of Lithium Dendrite Growth with Open-Source Software. *ACS Energy Letters* **2018**, *3*, 1737–1743.
- (22) Galib, M.; Orhan, O. K.; Liu, J.; Ponga, M. Residual stress development in lattice mismatched epitaxial thin films via atomic and molecular layer depositions. *Journal of the Mechanics and Physics of Solids* **2024**, *193*, 105897.
- (23) Diggle, J. W.; Despic, A. R.; Bockris, J. O. The Mechanism of the Dendritic Electrocrystallization of Zinc. *Journal of The Electrochemical Society* **1969**, *116*, 1503.
- (24) Srolovitz, D. On the stability of surfaces of stressed solids. *Acta Metallurgica* **1989**, *37*, 621–625.
- (25) He, H.; Liu, J. Suppressing Zn dendrite growth by molecular layer deposition to enable long-life and deeply rechargeable aqueous Zn anodes. *J. Mater. Chem. A* **2020**, *8*, 22100–22110.
- (26) Hosseini, S.; Abbasi, A.; Uginet, L.-O.; Haustraete, N.; Prasertdam, S.; Yonezawa, T.; Kheawhom, S. The Influence of Dimethyl Sulfoxide as Electrolyte Additive on Anodic Dissolution of Alkaline Zinc-Air Flow Battery. *Scientific Reports* **2019**, *9*, 14958.

- (27) Galib, M.; Orhan, O. K.; Ponga, M. Engineering Chemo-Mechanical Properties of Zn Surfaces via Alucone Coating. *The Journal of Physical Chemistry C* **2023**, *127*, 2481–2492.
- (28) Chen, L.; Zhang, H. W.; Liang, L. Y.; Liu, Z.; Qi, Y.; Lu, P.; Chen, J.; Chen, L.-Q. Modulation of dendritic patterns during electrodeposition: A nonlinear phase-field model. *Journal of Power Sources* **2015**, *300*, 376–385.
- (29) Hong, Z.; Ahmad, Z.; Viswanathan, V. Design Principles for Dendrite Suppression with Porous Polymer/Aqueous Solution Hybrid Electrolyte for Zn Metal Anodes. *ACS Energy Letters* **2020**, *5*, 2466–2474.
- (30) McLarnon, F. R.; Cairns, E. J. The Secondary Alkaline Zinc Electrode. *Journal of The Electrochemical Society* **1991**, *138*, 645–656.
- (31) Zuo, Y.; Wang, K.; Pei, P.; Wei, M.; Liu, X.; Xiao, Y.; Zhang, P. Zinc dendrite growth and inhibition strategies. *Materials Today Energy* **2021**, *20*, 100692.
- (32) Lu, W.; Xie, C.; Zhang, H.; Li, X. Inhibition of Zinc Dendrite Growth in Zinc-Based Batteries. *ChemSusChem* **2018**, *11*, 3996–4006.
- (33) Sang, L.; Ponga, M.; Fleischauer, M.; Wu, R. Navigating Solvent Chemistry and Microstructures: Toward Mechanically Enhanced Ceramic-Rich Composite Electrolytes. *The Journal of Physical Chemistry C* **2024**, *128*, 17240–17251.
- (34) Hao, F.; Verma, A.; Mukherjee, P. P. Mechanistic insight into dendrite–SEI interactions for lithium metal electrodes. *J. Mater. Chem. A* **2018**, *6*, 19664–19671.
- (35) Aagesen, L. K.; Gao, Y.; Schwen, D.; Ahmed, K. Grand-potential-based phase-field model for multiple phases, grains, and chemical components. *Phys. Rev. E* **2018**, *98*, 023309.

- (36) Wheeler, A. A.; Boettinger, W. J.; McFadden, G. B. Phase-field model for isothermal phase transitions in binary alloys. *Phys. Rev. A* **1992**, *45*, 7424–7439.
- (37) Kim, S. G.; Kim, W. T.; Suzuki, T. Phase-field model for binary alloys. *Phys. Rev. E* **1999**, *60*, 7186–7197.
- (38) Plapp, M. Unified derivation of phase-field models for alloy solidification from a grand-potential functional. *Phys. Rev. E* **2011**, *84*, 031601.
- (39) Choudhury, A.; Nestler, B. Grand-potential formulation for multicomponent phase transformations combined with thin-interface asymptotics of the double-obstacle potential. *Phys. Rev. E* **2012**, *85*, 021602.
- (40) Hötzer, J.; Jainta, M.; Steinmetz, P.; Nestler, B.; Dennstedt, A.; Genau, A.; Bauer, M.; Köstler, H.; Rüde, U. Large scale phase-field simulations of directional ternary eutectic solidification. *Acta Materialia* **2015**, *93*, 194–204.
- (41) Welland, M. J.; Tenuta, E.; Prudil, A. A. Linearization-based method for solving a multicomponent diffusion phase-field model with arbitrary solution thermodynamics. *Phys. Rev. E* **2017**, *95*, 063312.
- (42) Zhang, J.; Liu, Y.; Wang, C.; Tan, H. An Electrochemical-Mechanical Phase Field Model for Lithium Dendrite. *Journal of The Electrochemical Society* **2021**, *168*, 090522.
- (43) Kobayashi, R. Modeling and numerical simulations of dendritic crystal growth. *Physica D: Nonlinear Phenomena* **1993**, *63*, 410–423.
- (44) Cogswell, D. A. Quantitative phase-field modeling of dendritic electrodeposition. *Phys. Rev. E* **2015**, *92*, 011301.
- (45) Herring, C. Diffusional Viscosity of a Polycrystalline Solid. *Journal of Applied Physics* **1950**, *21*, 437–445.

- (46) McMeeking, R. M.; Ganser, M.; Klinsmann, M.; Hildebrand, F. E. Metal Electrode Surfaces Can Roughen Despite the Constraint of a Stiff Electrolyte. *Journal of The Electrochemical Society* **2019**, *166*, A984.
- (47) Ganser, M.; Hildebrand, F. E.; Klinsmann, M.; Hanauer, M.; Kamlah, M.; McMeeking, R. M. An Extended Formulation of Butler-Volmer Electrochemical Reaction Kinetics Including the Influence of Mechanics. *Journal of The Electrochemical Society* **2019**, *166*, H167.
- (48) Guerra, E.; Bestetti, M. Physicochemical Properties of $\text{ZnSO}_4 - \text{H}_2\text{SO}_4 - \text{H}_2\text{O}$ Electrolytes of Relevance to Zinc Electrowinning. *Journal of Chemical & Engineering Data* **2006**, *51*, 1491–1497.
- (49) Lindsay, A. D. et al. 2.0 - MOOSE: Enabling massively parallel multiphysics simulation. *SoftwareX* **2022**, *20*, 101202.
- (50) Adhikary, D. P.; Jayasundara, C.; Podgorney, R. K.; Wilkins, A. H. A robust return-map algorithm for general multisurface plasticity. *International Journal for Numerical Methods in Engineering* **2016**, *109*, 218–234.

Supporting Information

List of symbols

Table S1 outlines all the parameters applied in the current phase-field model discussed in the Theoretical Method section.

Theoretical Formulation of the Phase-Field Method

Table S1: Physical parameters (variables/constants) and their symbols

Parameter Name	Symbol	Parameter Name	Symbol
Order parameter	ξ	Electric potential	ϕ
Local electrochemical free energy density	$f_{\text{elec-ch}}$	Interfacial energy density	f_{in}
Elastic energy density	f_{ela}	Double well function	W
Gradient energy coefficient	κ	Langevin noise	f_{noise}
Anisotropic modulus	ω	Dendrite angle	θ
Heteroepitaxial compressive stress	σ_{f}	In-plane stress	σ_{film}
Interfacial stress	σ_{x}	Normal stress	σ_{y}
Modified chemical potential	μ	Chemical potential of deposited Zn	μ_0
Chemical potential of dendritic hump	μ_{hump}	Chemical potential of unperturbed system	μ^*
Activation overpotential	η_{α}	Standard equilibrium half cell potential	E^{θ}
Interfacial mobility	L_{σ}	Exchange current density	i_0
Electro-Chemical kinetic coefficient	L_{η}	Electrons transferred	n
Molar volume	V_m	Surface tension	γ
Gas constant	R	Charge transfer coefficient	α
Evolution time	t	Temperature	T
Molar fraction of Zn ion	$c_{\text{Zn}^{2+}}$	Molar fraction of Zn ion at t=0	c_0
Molar fraction of Zn in electrode	c^{l}	Molar fraction of Zn in electrolyte	c^{s}
Site density of electrode	C_{m}^{s}	Site density of electrolyte	C_{m}^{l}
Conductivity of electrode	σ^{s}	Conductivity of electrolyte	σ^{l}
Atomic volume	Ω_0	Interpolation function	$h(\xi)$
Zn electrode stiffness	C_{Zn}	Diffusivity of Zinc ion	D

The electrodeposition mechanism in Zn batteries is described by the electrochemical-mechanical phase field model (PFM). The Zn^{2+} ions transfer from the electrolyte to the zinc anode due to the electrochemical potential difference is replicated in this model. The Butler-Volmer equation is used to simulate how the accumulated Zn affects the evolution of the Zn-thin film interface (*i.e.*, moving upward) as electrodeposition proceeds.^{S34} However, to unveil the full potential of PFM, decoupling of interfacial energy and interfacial thickness is highly desirable to achieve a sufficiently good resolution of the interface,^{S35} which is a limitation for Wheeler, Boettinger, and McFadden's^{S36} pioneering alloy solidification model and Kim, Kim, and Suzuki's phase-field framework.^{S37} Here, we used an alloy solidification model developed by Plapp,^{S38} based on a grand-potential functional that preserves the benefit of decoupling interfacial thickness from interfacial energy while eliminating the necessity for variables of phase concentration in the chemical free energy term. Instead of composition, an evolution equation based on the difference in chemical potential among species is utilized, which has been used in several previous studies.^{S39-S41} The free energy functional for an electrochemical interface can be presented as:^{S42}

$$f(\xi, c_{\text{Zn}^{2+}}, \phi) = \int_V [f_{\text{elec-ch}}(\xi, c_{\text{Zn}^{2+}}, \phi) + f_{\text{in}}(\xi) + f_{\text{ela}}(\xi)] dV, \quad (\text{S1})$$

where ξ describes the transition from the electrolyte phase ($\xi = 0$) to the Zn solid phase ($\xi = 1$) and represents a non-conserved order parameter (phase-field variable); ϕ and $c_{\text{Zn}^{2+}}$ denote the electric potential and the Zn^{2+} cation concentration, respectively; $f_{\text{elec-ch}}(\xi, c_{\text{Zn}^{2+}}, \phi)$, $f_{\text{in}}(\xi)$, and $f_{\text{ela}}(\xi)$ are the local electrochemical free energy density, the interfacial energy density, and elastic energy density, respectively.

In the phase field model, the Zn anode's Ginzburg-Landau type heterogeneous interface energy density has the following form:

$$f_{in} = W(\xi) + \frac{1}{2}\kappa(\nabla\xi)^2 + f_{\text{noise}}. \quad (\text{S2})$$

The double well function, $W(\xi) = W_0(1 - \xi)^2\xi^2$ in Eq. (S2), characterizes the equilibrium states by defining the bulk energy needed to phase change from electrode to electrolyte (here, $W_0 = 2$ ^{S28}). Let κ be a gradient energy coefficient and $\frac{1}{2}\kappa(\nabla\xi)^2$ is the gradient energy density that correlates to the interface strength. f_{noise} measures the amount of interfacial heterogeneous deposition brought on by defects. On the anode interface, conserved Langevin noise is used to prevent concentration drift in simulations that ensure mass conservation. Langevin noise, f_{noise} , is incorporated into Eq. (S2) to consider the disturbance in the system caused by surface imperfections and thermal deviations that may initiate the development of the dendrite nucleus.

The gradient energy coefficient's anisotropy is expressed using Kobayashi's proposed formula as^{S43} $\kappa = \kappa_0[1 + \delta \cos(\omega\theta)]$. Here, ω is the anisotropic modulus which defines the number of preferential growth orientations of dendrites ($w = 6$ for hcp Zn^{S44}), θ is the angle between the crystallographic direction and the surface normal vector, and δ is the energy anisotropy coefficient/strength of anisotropy of hexagonal close-packed Zn crystal. It is a microscopic interaction width that affects the interface's movement to add anisotropy by considering that δ relies on the orientation of the interface's outer normal vector.

To characterize the stress effect during plating, the elastic energy density is introduced:

$$f_{\text{ela}}(\xi) = \frac{1}{2}C_{\text{Zn}}\epsilon_{\text{Zn}}^2, \quad (\text{S3})$$

where the effective stiffness of zinc solid is represented by C_{Zn} (assumed isotropic in this case). For calculating f_{ela} , the equilibrium equation of solid is solved to depict the stress-strain behavior by solving for displacement field \mathbf{u} in the domain Ω_A , which has the following strong form: $\nabla \cdot \boldsymbol{\sigma} + \mathbf{b} = 0$ in Ω_A , where $\boldsymbol{\sigma}$ denotes the Cauchy stress tensor and \mathbf{b} denotes the body force. The finite strain increment, total strain, and incremental rotation are computed for the generic time (t) increment such that $t \in [t_n, t_{n+1}]$. The resulting strain is calculated referencing the deformed arrangement (*i.e.*, Eulerian definition) using the Eulerian-Almansi

finite strain tensor as $\boldsymbol{\varepsilon}_{\text{Zn}} = \frac{1}{2}(I - \hat{\mathbf{C}}^{-1})$. Here, $\hat{\mathbf{C}} = \hat{\mathbf{F}}\hat{\mathbf{F}}^T$ is incremental right Cauchy-Green deformation tensor, $\hat{\mathbf{F}} = \frac{\partial \mathbf{x}_{n+1}}{\partial \mathbf{x}_n} = \mathbf{F}_{n+1}\mathbf{F}_n^{-1}$; $\hat{\mathbf{F}}$ is incremental deformation gradient, and \mathbf{F}_n is the total deformation gradient at time t_n ; \mathbf{x} is the position vector ($\mathbf{x}_{n+1} = \mathbf{x}_n + \mathbf{u}$).

Developed heteroepitaxial residual compressive stresses (σ_f)^{S22} in the thin film are implemented leveraging the diffused interface between the two phases in phase field model as the interface stress as shown in Fig. 1 (b) of the manuscript and defined by the gradient of an order parameter as $\boldsymbol{\sigma}_{\text{film}} \cdot f(|\nabla\xi|)$. Therefore, the 2D stress tensor, $\boldsymbol{\sigma}_{\text{film}} = (\mathbf{Q} \cdot \mathbf{M} \cdot \mathbf{Q}^{-1})$, and $f(|\nabla\xi|) = |\nabla\xi|$, where $\mathbf{M} = \begin{pmatrix} 0 & 0 \\ 0 & \sigma_f \end{pmatrix}$, $\mathbf{Q} = (\vec{e}_1 \ \vec{e}_2)$. Here, \mathbf{Q} and \mathbf{Q}^{-1} are applied as the basis transformation from the eigenvector basis to the cartesian basis. $\vec{e}_1 = \frac{\nabla\xi}{|\nabla\xi|}$ eigenvector is applied in the direction of the order parameter gradient as shown in Fig. 1(b), with an eigenvalue of zero, whereas \vec{e}_2 is perpendicular to that direction.

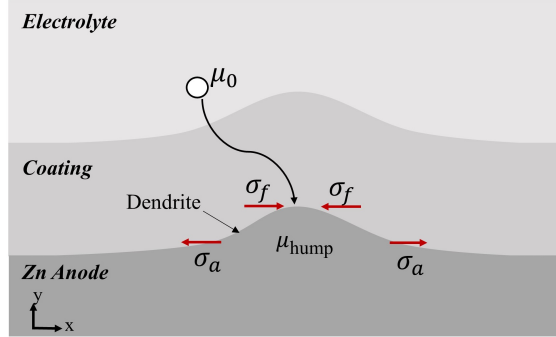


Figure S1: Schematic diagram illustrating impact of thin-film/coating (σ_f) and anode stress (σ_a) on chemical potential. Relative sizes not at scale in the schema.

From Fig. S1, assuming the humps form during plating in the anode with an addition of δN atoms with δv volume change to the Zn crystal, the work done to add the new atoms will be $(\mu^* - \mu_{\text{hump}} - \mu_0) \delta N$; where μ^* , μ_{hump} and μ_0 are chemical potential of the unperturbed system, dendritic hump and deposited Zn ions, respectively. If the free energy of the hump is δF , we can write the work done as $(\delta F - \mu_0 \delta N - \sigma_x \delta v - \sigma_y \delta v)$, where σ_x and σ_y are interfacial (due to hetero-epitaxy)^{S22} and normal stresses on the surface. Here, $\mu_0 \delta N$ denotes the Zn ions bulk reference energy, and we assume $\delta F = \mu_0 \delta N$ for a stable

hump without any spontaneous desolvation. Therefore, by equating these two works, we get $\mu^* - \mu_{\text{hump}} = \mu_0 - \sigma_x \Omega_0 - \sigma_y \Omega_0$, ^{S45} where $\Omega_0 = \delta v / \delta N$ is the atomic volume. Therefore, the modified chemical potential along a heteroepitaxial thin film anode interface, μ , is:

$$\mu = \mu_0 - \sigma_x \Omega_0 - \sigma_y \Omega_0. \quad (\text{S4})$$

Here, the interfacial stress (σ_x) is related to interfacial tension as $-\sigma_x = \gamma \Omega_0 K(x)$. ^{S24} Additionally, γ is the interfacial tension, Ω_0 denotes the atomic volume, and $K(x)$ refers to the curvature of the interface. The second term on the right-hand side of Eq. (S4) reflects the contribution of surface energy to the chemical potential. The third component quantifies the impact of stress, which is perpendicular to the interfacial contact, on the release or absorption of an atom at that interface.

Therefore, to add the effect of modified chemical potential in the electrochemical free energy density ($f_{\text{elec-ch}}(\xi, c_{\text{Zn}^{2+}}, \phi)$), the activation over-potential (η_α) has to be modified. η_α can be written as $\eta_\alpha = \phi - E^\theta$, E^θ is the standard equilibrium half-cell potential of the electrode relative to the electrolyte, and $\phi = \phi^{\text{etrode}} - \phi^{\text{elyte}}$ is the applied over-potential. Here, ϕ^{etrode} is the potential in the electrode neighboring to the interfacial region, and ϕ^{elyte} is the electrolyte potential adjacent to that interface. Ganser *et al.* presented the equilibrium cell potential as ^{S46,S47}

$$\begin{aligned} FE^\theta &= \mu^{\text{elyte}} - \mu^{\text{etrode}} \\ &= \mu_0^{\text{elyte}} - \mu_0^{\text{etrode}} - \sigma_x \Omega_0 - \sigma_y \Omega_0 \\ &= FE_0^\theta - \sigma_x \Omega_0 - \sigma_y \Omega_0, \end{aligned} \quad (\text{S5})$$

where μ^{etrode} refers to the chemical potential of the Zn metal ion specifically in the electrode, and μ^{elyte} is in the electrolyte. Here, F denotes the Faraday constant ($F = 96485 \text{ C} \cdot \text{mol}^{-1}$) and $\mu^{\text{elyte}} = \mu_0^{\text{elyte}}$; neglecting the contribution of stress to the the chemical potential of the Zn ion in the electrolyte. These chemical potentials can be controlled by stress as shown in Eq. (S4), just as they can be by any other non-ideality or departure from a datum state.

Using Eq. (S5), we can write the η_α as

$$\eta_\alpha = (\phi^{\text{etrode}} - \phi^{\text{elyte}} - E_0^\theta) + (\sigma_x + \sigma_y) \frac{\Omega_0}{F}. \quad (\text{S6})$$

For the electrochemical reaction in the anode ($\text{Zn}^{2+} + 2e^- \rightleftharpoons \text{Zn}$), the spatial evolution of free energy density ($f_{\text{elec-ch}}(\xi, c_{\text{Zn}^{2+}}, \phi)$) with respect to ξ ($\frac{\partial f_{\text{elec-ch}}}{\partial \xi}$) coupled with the solid and ions phases of Zn and the overpotential η_α takes the following shape

$$\begin{aligned} \Gamma &= \frac{\partial f_{\text{elec-ch}}}{\partial \xi} \\ &= \left\{ \exp \left[\frac{(1-\alpha)nF\eta_\alpha}{RT} \right] - \frac{c_{\text{Zn}^{2+}}}{c_o} \exp \left[\frac{-\alpha nF\eta_\alpha}{RT} \right] \right\} \\ &= \left\{ \exp \left[\frac{(1-\alpha)nF(\phi - E_0^\theta) + (1-\alpha)\Omega_0(\sigma_x + \sigma_y)}{RT} \right] \right. \\ &\quad \left. - \frac{c_{\text{Zn}^{2+}}}{c_o} \exp \left[\frac{-\alpha nF(\phi - E_0^\theta) - \alpha\Omega_0(\sigma_x + \sigma_y)}{RT} \right] \right\}. \end{aligned} \quad (\text{S7})$$

In the electrodeposition case, under high overpotential when the cathodic reaction current is much smaller than the anodic reaction current, Eq. (S7) can be simplified by neglecting the mechanical contribution to the cathodic reaction current,

$$\Gamma = \left\{ \exp \left[\frac{(1-\alpha)nF\eta_\alpha}{RT} \right] - \frac{c_{\text{Zn}^{2+}}}{c_o} \exp \left[\frac{-\alpha nF\eta_\alpha - \alpha\Omega_0(\sigma_x + \sigma_y)}{RT} \right] \right\}. \quad (\text{S8})$$

The temporal growth of the phase-field variable ξ in Eq. (S1) using classical Butler-Volmer

equation can be expressed as [S21,S28,S29](#)

$$\begin{aligned}
\frac{\partial \xi}{\partial t} &= -L \frac{\partial f(\xi, c_{\text{Zn}^{2+}}, \phi)}{\partial \xi} \\
&= -L \left[\frac{\partial f_{\text{in}}(\xi) + \partial f_{\text{ela}}(\xi)}{\partial \xi} + \Gamma \right] + f_{\text{noise}} \\
&= -L_{\sigma} (W'(\xi) - \kappa \nabla^2 \xi) - L_{\sigma} \frac{\partial f_{\text{ela}}(\xi)}{\partial \xi} - L_{\eta} h'(\xi) \left\{ \exp \left[\frac{(1 - \alpha)nF\eta_{\alpha}}{RT} \right] \right. \\
&\quad \left. - \frac{c_{\text{Zn}^{2+}}}{c_0} \exp \left[\frac{-\alpha nF\eta_{\alpha}}{RT} \right] \exp \left[\frac{-\alpha(\sigma_x + \sigma_y)\Omega_0}{RT} \right] \right\} + f_{\text{noise}}.
\end{aligned} \tag{S9}$$

Here, L_{σ} refers to the interfacial mobility activities ($2.5 \times 10^{-7} \text{ m}^3 \cdot \text{J}^{-1} \cdot \text{s}^{-1}$) [S29](#) and $L_{\eta} = \frac{V_m \gamma}{F\kappa} i_0$ refers to the electro-chemical kinetic coefficient. From Eq. (S9), V_m , i_0 , γ , α , n , R , t , and T are the molar volume of Zn (9.16 cm^3), [S44](#) the exchange current density (varies from $1.5 - 5 \text{ mA} \cdot \text{cm}^{-2}$ in this study), surface tension ($0.5 \text{ J} \cdot \text{m}^{-2}$), [S44](#) charge-transfer coefficient (fixed to 0.5 in this study), number of electrons transferred (2 for Zn electrodeposition), gas constant ($R = 8.314 \text{ J} \cdot \text{mol}^{-1} \cdot \text{K}^{-1}$), evolution time, and temperature (300 K), respectively. Note that the value for Langevin noise (f_{noise}) was fixed to 0.04 for this study. The interfaces between the electrode and electrolyte have a finite thickness, where the value of ξ lies between 0 and 1. Here, a polynomial tilting/interpolation function $h(\xi) = \xi^3(6\xi^2 - 15\xi + 10)$ [S28](#) is used for smoothly interpolating different physical parameters between two phases. Its derivative, $h'(\xi) = 30\xi^2(1 - \xi)^2$, is only valid at the interface as h' becomes zero when ξ proceed towards 0 or 1. Therefore, using $h'(\xi)$ for interpolation of physical parameters ensures that the electrochemical reactions occur solely at the interface. The variables $c_{\text{Zn}^{2+}}$ and c_0 represent the molar ratios of zinc ions at a particular location and at the beginning (at $t = 0 \text{ s}$, $\frac{1}{c_0} = 58.556$), respectively. Here, $c_{\text{Zn}^{2+}}$ can be expressed as [S44](#)

$$c_{\text{Zn}^{2+}} = c^{(1,s)}(1 - h(\xi)) = \frac{\exp \left[\frac{(\mu_0 - \epsilon^{(1,s)})}{RT} \right]}{1 + \exp \left[\frac{(\mu_0 - \epsilon^{(1,s)})}{RT} \right]} (1 - h(\xi)), \tag{S10}$$

The variables c^l and c^s represent the molar fraction of Zn in the electrolyte and electrode

phase, respectively. The term $\epsilon^{(l,s)} = \mu_0^{(l,s)} - \mu_0^{N_0}$ refers to the difference in the chemical potential of Zn and neutral elements in the electrolyte at the initial equilibrium condition.

The chemical potential (μ_0) of the Zn ions can be derived from the mass conservation law, as:^{S29}

$$\chi \frac{\partial \mu_0}{\partial t} = \nabla \cdot \frac{D c_{\text{Zn}^{2+}}}{RT} [\nabla \mu_0 + nF \nabla \phi] - \frac{\partial h(\xi)}{\partial t} \left[c^s \frac{C_m^s}{C_m^l} - c^l \right], \quad (\text{S11})$$

where the susceptibility factor $\chi = \frac{\partial c^l}{\partial \mu_0} [1 - h(\xi)] + \frac{\partial c^s}{\partial \mu_0} h(\xi) \frac{C_m^s}{C_m^l}$ and D is the diffusivity ($3.68 \times 10^{-10} \text{ m}^2 \cdot \text{s}^{-1}$).^{S44} Therefore, μ_0 can be determined from the revised diffusion equation Eq. (S11) where C_m^s ($1.092 \times 10^5 \text{ mol} \cdot \text{m}^{-3}$)^{S44} and C_m^l ($5.652 \times 10^4 \text{ mol} \cdot \text{m}^{-3}$)^{S29} represent the electrode and electrolyte site densities which are inverse of molar volume. The distribution of ϕ over the spatial domain can be acquired from the effective conductivity (σ^c), i.e., from conduction equation^{S21}

$$\nabla \sigma^c \nabla \phi = nF C_m^s \frac{\delta(\xi)}{\delta t}. \quad (\text{S12})$$

Here, σ^c is determined by the conductivity of the electrode phase, σ^s ($10^7 \text{ S} \cdot \text{m}^{-1}$),^{S29} and the conductivity of the electrolyte phase, σ^l ($4.64 \text{ S} \cdot \text{m}^{-1}$ for 1 M of ZnSO_4)^{S48} and can be expressed as $\sigma^c = \sigma^s h(\xi) + \sigma^l [1 - h(\xi)]$.

Computational Implementation

In this study, we utilized the open-source MOOSE software^{S49,S50} to develop the grand potential-based nonlinear phase-field model. This model investigated a set of coupled nonlinear equations (*i.e.*, phase-field equation coupled with chemical potential and conduction equations) to understand the effect of the thin film-deposited residual stress on electrodeposition kinetics. The phase-field model computes the changes across time and space of three

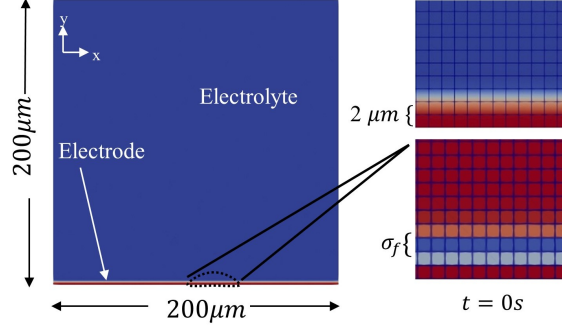


Figure S2: Diagram illustrating the simulated cell's initial frame prior to electrodeposition and the mesh size.

independent variables (ξ, μ, ϕ) . In MOOSE, Eq. (S9), Eq. (S10), Eq. (S11) and Eq. (S12) are converted to its weak form and solved simultaneously by minimizing the total residual. The coupled variables were normalized to ensure that they weighed almost equally. Here, the coupling between the variables is as follows: the phase-field variable ξ of Eq. (S9) relies on variable μ via the local zinc-ion molar fraction using Eq. (S10). Secondly, based on Eq. (S11), it can be deduced that μ is influenced by ϕ from Eq. (S12) and ξ from Eq. (S9), whereas ϕ in Eq. (S12) only depends on ξ . To maintain the accuracy of the boundary conditions, the cutoff distance is established at a value that is less than 90% of the simulation size. The initial geometry before starting the first plating at $t = 0$ s displayed in Fig. S2 is illustrated by the distribution of ξ in the following equation

$$\xi(x, y) = \frac{1 - \tanh[2(x - 2)]}{2}, \quad (\text{S13})$$

which denotes the anode thickness of $2 \mu\text{m}$ with a smooth shift at the interface from the anode to the electrolyte. The remaining $198 \mu\text{m}$ is occupied by the electrolyte in a $200 \mu\text{m} \times 200 \mu\text{m}$ domain as shown in Fig. S2. The electric potential ϕ is initially specified as $\phi(x, y) = \phi_{\text{applied}} \xi(x, y)$ such that the anode and electrolyte have the potential of ϕ_{applied} and 0, respectively, at $t = 0$ s. ϕ_{applied} represents the overpotential applied over the interface. The chemical potential (μ) was also set to zero at $t = 0$ s for the whole domain. The spatial distribution of all independent variables (ξ, μ, ϕ) are resolved using Newton-Raphson's

iterative approach at 0.01 s time step along with adaptive time steps. Here, we normalized the parameters (time, length, temperature, and stress) using the following normalization factors: 1 s, 1 μm , 1 K, and 1×10^9 Pa, respectively. All post-processing and analysis of the MOOSE simulations has been performed using the open-source Python package called "MOOSEanalyze".

Results

In-situ optical microscopy for multiple coated layers

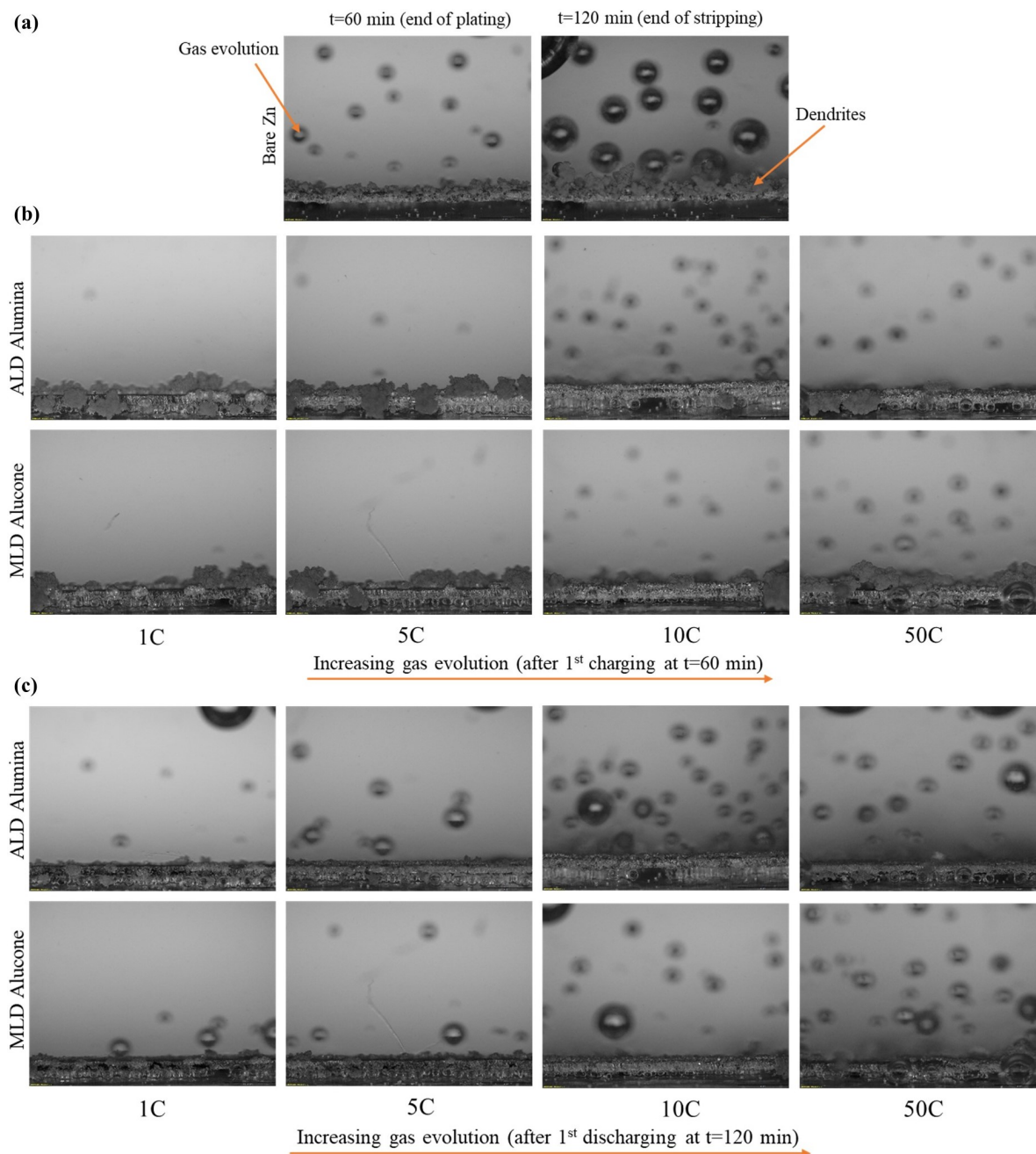


Figure S3: Gas evolution observation from in-situ optical microscopy at $i = 10 \text{ mA} \cdot \text{cm}^{-2}$ (a) bare Zn, (b) charging states for coated Zn at $t = 60$ min, and (c) discharging stages for coated Zn at $t = 120$ min.

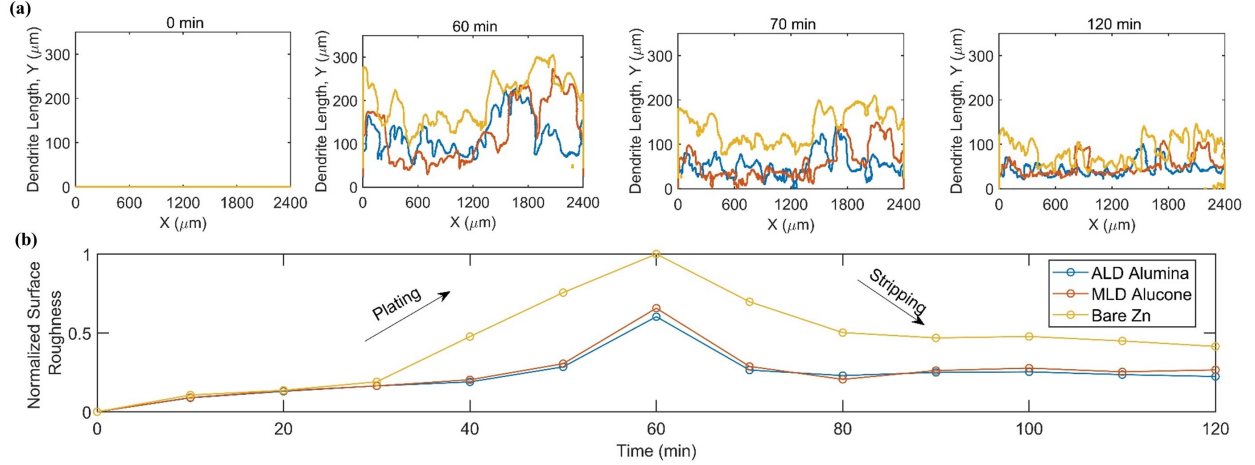


Figure S4: (a) dendrite profile extracted during plating (0, 60 min) and stripping (70, 120 min); and (b) normalized surface roughness with time for coated and bare Zn.

Cyclic test for multiple coated layers

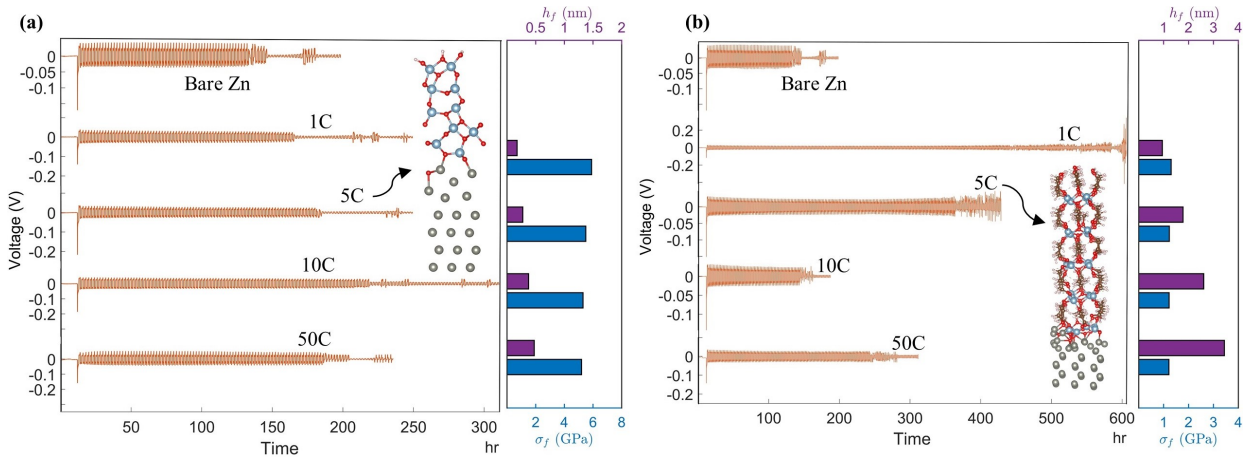


Figure S5: Charging/discharging cycles for Bare and coated Zn at different coating thicknesses (1C, 5C, 10C, 50C) with their corresponding hetero-epitaxial stress for (a) ALD Alumina, (b) MLD Alucone. Color code for the atoms in 5C alumina & alucone: carbon - brown, zinc - gray, aluminium - blue, hydrogen - pink, and oxygen - red.

In Fig. S5, one (1C), five (5C), ten (10C), and fifty (50C) coated layers of ALD alumina and MLD alucone were cycled to understand the effect of coating thickness on cyclic life. Here, the coating thickness (h_f) and lattice misfit (ϵ_m) were measured from density functional theory (DFT) optimized structures^{S27} as shown in the inset of Fig. S5(a), (b) for 5C case. Then, the coating generated hetero-epitaxial stress is calculated using the analytical formulation:

$\sigma_f = \frac{\varepsilon_m}{\left(\frac{1}{MT} + \frac{4h_f}{h_s M}\right)}$ ^{S22} using their stiffness properties (M) ^{S27} and Zn foil thickness ($h_s = 0.1\text{mm}$). The range of interfacial compressive stress is found to be 5.2-5.9 GPa for ALD Alumina and 1.2-1.3 GPa for MLD Alucone, which is the applied initial interfacial stress in our phase-field formulation.

Chemical potential evolution

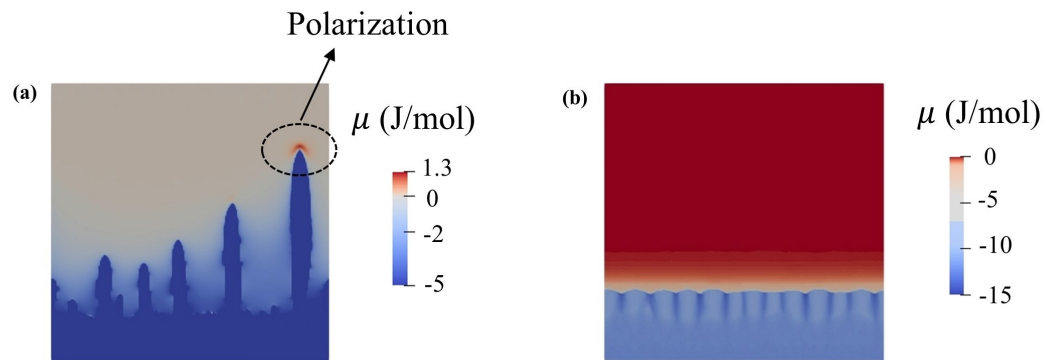


Figure S6: The change in chemical potential (μ) at a applied overpotential (ϕ) of 200 mV, current density (i) of ($2.8 \text{ mA} \cdot \text{cm}^{-2}$) and anisotropy (δ) of 0.0 at 150 seconds, respectively, for : (a) bare Zn, and (b) coated Zn.